Supporting Information: Shear Banding in Entangled Polymers: Stress Plateau, Banding Location, and Lever Rule

Yongjin Ruan,[†] Yuyuan Lu,[*,†] Lijia An,[*,†] and Zhen-Gang Wang[*,‡]

†*State Key Laboratory of Polymer Physics and Chemistry, Changchun Institute of Applied Chemistry, Chinese Academy of Sciences, Changchun 130022, People's Republic of China*

‡*Division of Chemistry and Chemical Engineering, California Institute of Technology, Pasadena, California 91125, United States*

E-mail: yylu@ciac.ac.cn; ljan@ciac.ac.cn; zgw@caltech.edu

S1 Simulation details for the Kremer–Grest (KG) model

In this work, we use the KG model[S1] with a bending potential[S2] at a monomer density of $\rho = 0.85d^{-3}$. All monomers are modeled as beads interacting through a truncated and shifted 12-6 Lennard-Jones (LJ) potential,

$$U_{\mathrm{LJ}} = 4\epsilon[(d/r_{ij})^{12} - (d/r_{ij})^{6} + 1/4]\Theta((r_{\mathrm{c}} - r_{ij})/d) \tag{S1}$$

where d is the LJ diameter, r_{ij} is the distance between monomer i and j, $r_{\mathrm{c}} = 2^{\frac{1}{6}}d$ is cut-off distance, and $\Theta(x)$ is the Heaviside step function (with $\Theta(x) = 0$ for $x < 0$ and $\Theta(x) = 1$ for $x \geq 0$). Chain connectivity is modeled by the finitely extensible nonlinear elastic (FENE)

potential between adjacent monomers on the chain,

$$U_{\mathrm{FENE}} = -\frac{k}{2} R_0^2 \ln[1 - (r/R_0)^2] \tag{S2}$$

where the spring constant $k = 30\epsilon/d^2$ and fully stretched bond length $R_0 = 1.5d$. The bending potential between two consecutive bonds along the chain is taken to be of the form[S2]

$$U_{\mathrm{bend}} = k_{\mathrm{b}}(1 - \cos\theta) \tag{S3}$$

with $k_{\mathrm{b}} = 2\epsilon$, and has the effect of increasing the entanglement density with the same chain length.

Length, energy, and time are nondimensionalized respectively by the monomer diameter d, energy parameter ϵ, and the LJ timescale $\tau = (md^2/\epsilon)^{1/2}$, where m is the monomer mass set to be 1. The temperature is chosen such that $\epsilon/k_{\mathrm{B}}T = 1$ and is controlled by the DPD thermostat[S3–S5]: the force $\boldsymbol{F}_{ij}$ exerted on particle i by particle j is composed of conservative ($\boldsymbol{F}_{ij}^{\mathrm{C}}$, from LJ and FENE potentials), dissipative ($\boldsymbol{F}_{ij}^{\mathrm{D}}$) and random ($\boldsymbol{F}_{ij}^{\mathrm{R}}$) forces,

$$\boldsymbol{F}_{ij}^{\mathrm{D}} = -\xi\omega^{\mathrm{D}}(r_{ij})(\hat{\boldsymbol{r}}_{ij} \cdot \boldsymbol{v}_{ij})\hat{\boldsymbol{r}}_{ij} \tag{S4}$$

$$\boldsymbol{F}_{ij}^{\mathrm{R}} = \mu\omega^{\mathrm{R}}(r_{ij})\theta_{ij}\hat{\boldsymbol{r}}_{ij} \tag{S5}$$

where $\boldsymbol{r}_{ij} = \boldsymbol{r}_i - \boldsymbol{r}_j$ and $\boldsymbol{v}_{ij} = \boldsymbol{v}_i - \boldsymbol{v}_j$ are respectively the relative distance and velocity between monomers i and j, and $\hat{\boldsymbol{r}}_{ij} = \boldsymbol{r}_{ij}/|\boldsymbol{r}_{ij}|$ is the unit vector. The noise strength μ and friction coefficient ξ are related by $\mu^2 = 2\xi k_{\mathrm{B}}T$ and $\xi = 0.5$. The $\theta_{ij}(t)$ function is a symmetric Gaussian random variable with zero mean and unit variance. When $r < r_{\mathrm{c}}$, the weight function $\omega^{\mathrm{D}}(r) = [\omega^{\mathrm{R}}(r)]^2 = (1 - r/r_{\mathrm{c}})^2$; otherwise it is zero. The simulation time step is 0.005τ. Figs. S1(a), (b), and (c) show the scaling of the equilibrium mean-square radius of gyration R_{g0}^2, center of mass diffusivity D, and disengagement time τ_{d0}, respectively. The disengagement time τ_{d0} is obtained from fitting the time correlation function of the unit

end-to-end vector to the Kohlrausch–Williamson–Watts equation $C(t) = \exp[(-t/\alpha)^{\beta}]$ which yields $\tau_{d0} = \frac{\alpha}{\beta}\Gamma(\frac{1}{\beta})$ where Γ is the Gamma function.[S6] We estimate the Rouse time τ_R by $\tau_{d0} = 3Z\tau_R(1 - 3.38/Z^{0.5} + 4.17/Z - 1.55/Z^{1.5})$, as derived by Likhtman and McLeish.[S7] For $N = 300$, we find $\tau_{d0} = 3.67 \times 10^6\tau$ and $\tau_R = 2.4 \times 10^5\tau$. With the mean-square end-to-end distance $R^2_{e0} = 972.0$ (see Fig. S2) and the average bond length $l = 0.964$[S2], the Flory characteristic ratio is $C_\infty = R^2_{e0}/(N-1)l^2 = 3.50$.

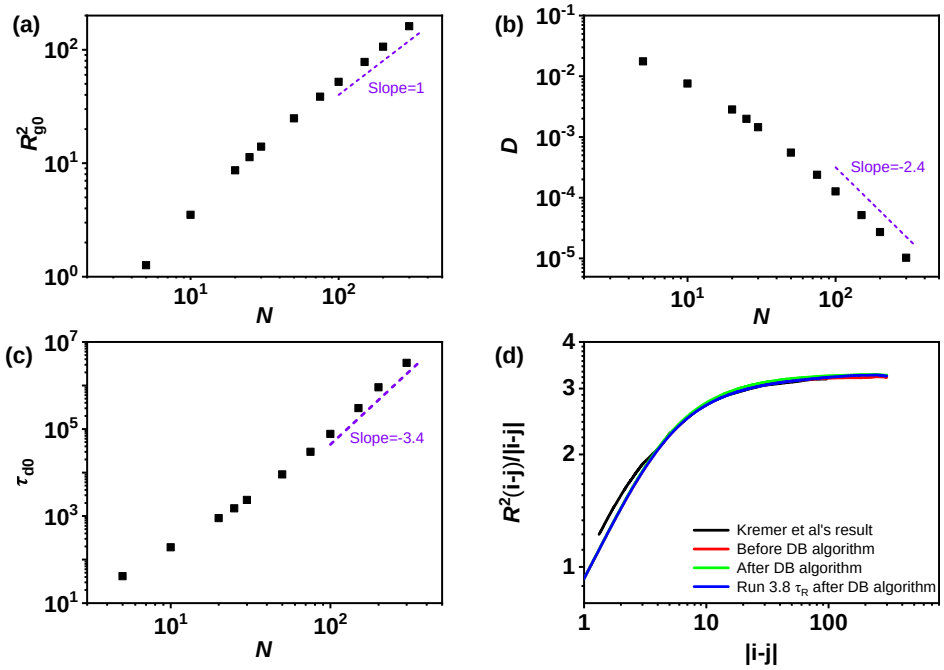

Figure S1: (a) Mean-square radius of gyration, (b) center-of-mass diffusivity, and (c) disengagement time as a function of the chain length at equilibrium. (d) The mean square internal distances using different equilibration protocols, compared with data from Ref. S2 (black curve). Data from Ref. S2 were reproduced with permission from AIP Publishing, Copyright 2003.

We initialized the system by lattice Monte Carlo sampling[S8] allowing chain crossing to achieve rapid entanglement of the chains. We then subjected the system to the potentials used in this work and further equilibrated the system for a duration of the disengagement time τ_{d0}. Since the double-bridging-MD hybrid algorithm[S2] is a standard and rapid method for equilibration in dense polymers, we also implemented this algorithm to the sample obtained above at three stages, each lasting 2.3×10^7 steps ($\sim 0.5\tau_R$), with the spring constant k increasing from 10 to 20 to 30. After this process, further equilibration is performed for

1.8×10^8 steps ($\sim 3.8\tau_{\rm R}$). Fig. S1(d) shows the mean square internal distances at different time.

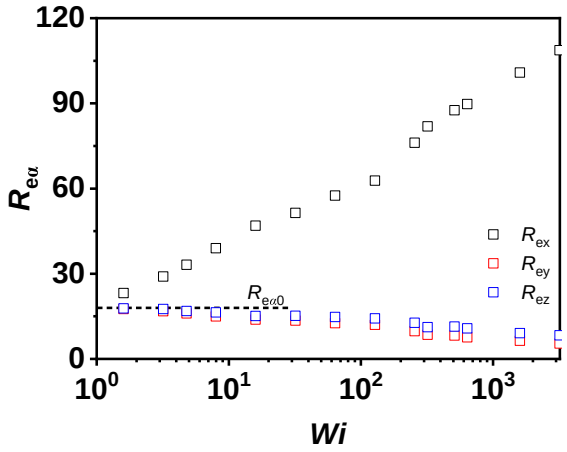

Figure S2: Components of the end-to-end distance in steady shear. R_{ex}, R_{ey}, and R_{ez} are the components in flow, gradient, and vorticity directions, respectively. The equilibrium value is $R_{e\alpha 0} = \sqrt{R_{e0}^2/3} = 18.0$, for x, y, and z.

The steady shear stress is calculated from the instantaneous stress using stored conformations after shearing the system for time t_0 (strain γ_0). t_0 (γ_0) is determined from visual inspection of the stress–time and stress–strain curves such as shown from Figs. S3(a) and (b). Table S1 lists t_0, γ_0, the total shearing time $t_{\rm run}$, and total strain $\gamma_{\rm run}$ for the different shear rates. The instantaneous stress data are the results of smoothing over 1700τ. The steady shear stress shown in Fig. 1 of the main text is obtained by averaging from time t_0 to $t_{\rm run}$, further averaged over the 8 independent samples. The square root of the three components of the mean-square end-to-end distance in steady shear, $R_{e\alpha} \equiv \langle R_{e\alpha}^2 \rangle^{1/2}$, is shown in Fig. S2.

Table S1: List of simulation time (unit: $\tau_{\rm d0}$) and strain.

Wi	1.6	3.2	4.8	8.0	16.0	31.9	63.8	128	256	319	511	638	1597	3193
$t_{\rm run}$	2.5	2.2	2.1	4.4	2.2	9.0	1.1	9.0	0.4	4.7	0.2	0.2	0.18	0.09
$\gamma_{\rm run}$	4	7	10	35	35	290	70	1150	110	1500	110	150	270	300
t_0	1.0	1.0	1.0	1.0	1.0	1.0	0.5	1.0	0.2	1.0	0.1	0.1	0.1	0.05
γ_0	1.6	3.2	4.8	8.0	16	32	32	120	50	320	50	60	160	160

The kink number per chain $Z_{\rm k}$ is calculated by the Z1 code when the simulation box happens to be a cuboid. We provide the LAMMPS in-file for the KG model as additional

Supporting Information material. The chain coordinate data are available from the corresponding authors on reasonable request.

S2 Evolution of stress and velocity profiles

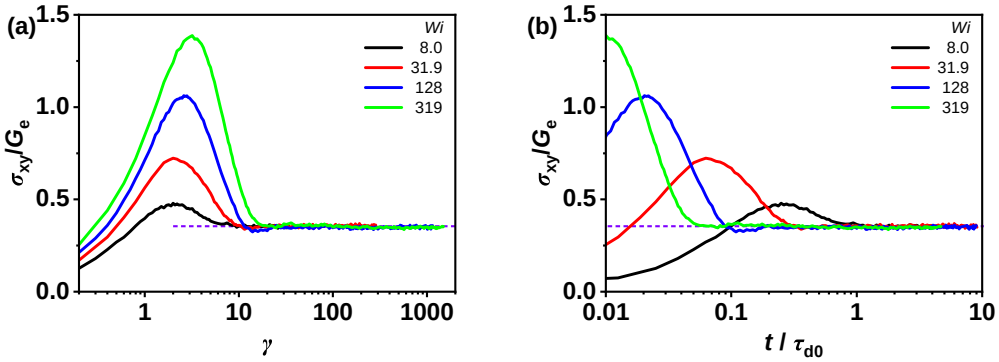

Figure S3: (a) Stress–strain curves and (b) stress–time curves for $Wi = 8.0$, 31.9, 128, and 319.

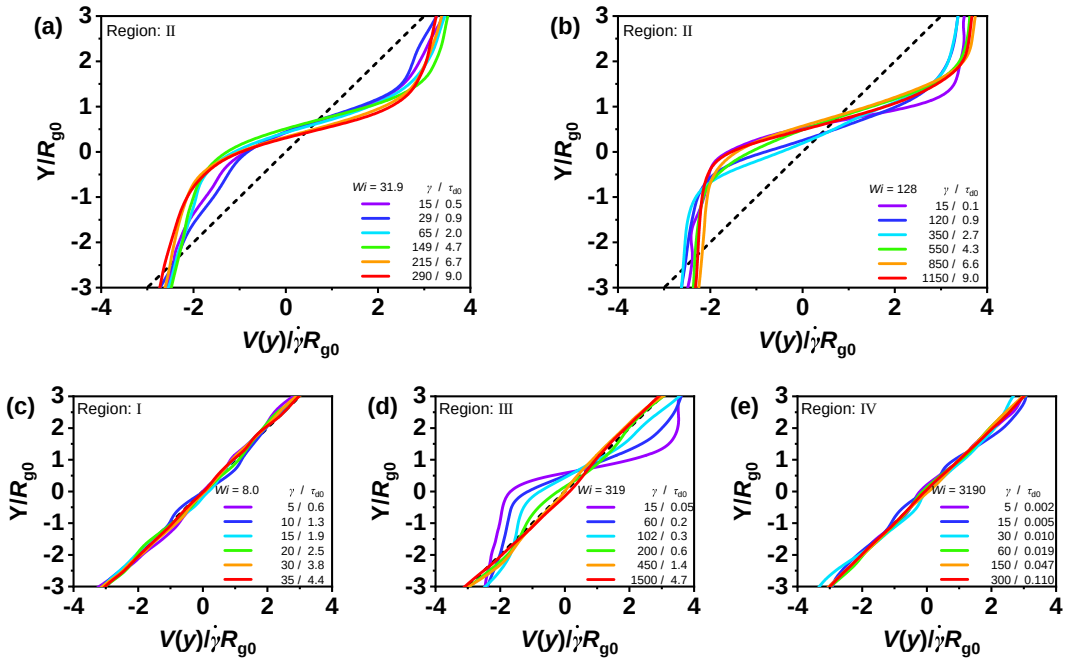

Figure S4: Velocity profiles for $Wi = 8.0$, 31.9, 128, 319, and 3190 at different times (strains). For $Wi = 31.9$ and $Wi = 128$, the shear bands are stable and persistent to the longest simulation time $t = 9.0\tau_{d0}$. For $Wi = 319$, the shear bands are transient. The dash line is the linear velocity profile for reference.

S3 Three special transient velocity profiles

At earlier times, one system showed a recoil-like motion in the slower band (Fig. S5(a)). Then, the slow band appears to reach zero shear rate, suggesting a "plug flow" behavior (Fig. S5(b)). These are transient behaviors that disappear with increasing strain. Some systems show more than two shear bands during the startup shear, which then coalesce to two larger, more pronounced shear bands with time (Fig. S5(c)). These transient behaviors have been reported in experiment[S9] and numerical simulation with a continuum model.[S10]

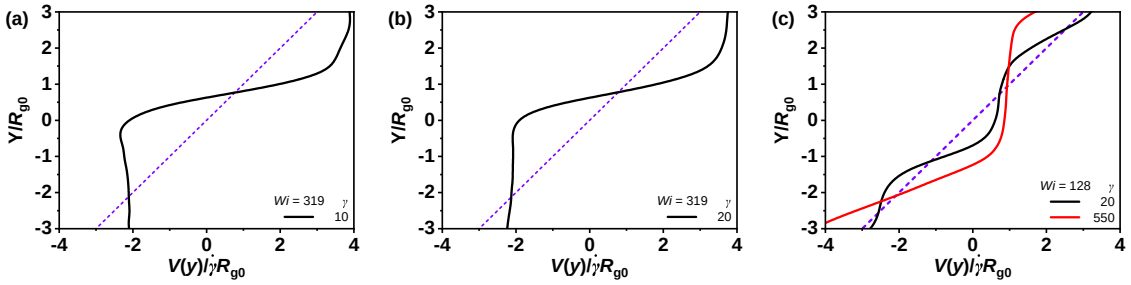

Figure S5: Special velocity profiles of a single sample: (a) recoil-like motion, (b) "plug flow" behavior, and (c) multiple (black) and two (red) bands. The purple dash line is the linear velocity profile.

S4 Determination of the shear rates in the fast and slow bands and the location of the band interface

Because the lever rule is based on analogy with liquid–gas coexistence, we performed simulation of liquid–gas coexistence in a Lennard-Jones liquid[S11] in order to assess the effects of finite interfacial widths and finite system size on the lever rule. For our LJ fluids, the particles interact through Eq. S1, but the cut-off distance is now $r_c = 4.0d$ to include attraction. The temperature is controlled by the Nosé–Hoover thermostat.[S12] To make the liquid–gas separation along the z direction[S13], the box size should be larger in z direction. We set the box size $L_x : L_y : L_z = 1 : 1 : 1.5$, $1 : 1 : 2$, and $1 : 1 : 3$ with the periodic boundary condition and performed simulations at two overall densities, $\rho_{\text{ave}} = 0.3$ and $\rho_{\text{ave}} = 0.2$. The number of particles ranges from 3072 to 6144, and the actual system dimension is $L_x \approx 20$ (with small variations to accommodate the specified density and integer particle number).

Following Ref. S11, we initialized the particle configuration on a FCC lattice with the average density. We first set the temperature $T = 0.5$ and run for 400τ, then increased T to 0.9 and run for 1200τ to reach an equilibrium density distribution.

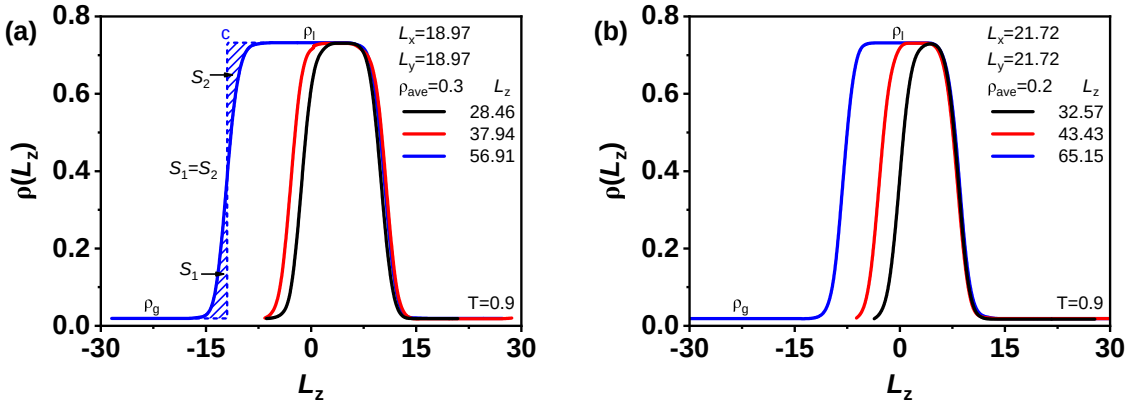

Figure S6: Density profile for liquid–gas coexistence at different system sizes, (a) $\rho_{\text{ave}} = 0.3$ and (b) $\rho_{\text{ave}} = 0.2$. Line c is Gibbs dividing surface, which makes the shaded areas $S_1 = S_2$.

Fig. S6 shows the density profile along the z direction at $\rho_{\text{ave}} = 0.3$ and 0.2. The density of the liquid (ρ_{l}) and gas (ρ_{g}) phases are essentially unchanged with the system size and overall density. For the larger box sizes and higher overall density, there are clear regions of uniform liquid and gas density. For the smallest system size and lower density, the range of the uniform liquid density nearly vanishes, but the density maximum is still very close to the liquid density for the larger systems. To locate the interface between the liquid and gas, we use the Gibbs equal area construct[S14] as shown in Fig. S6(a) for the density profile in blue. Equality of the shade areas $S_1 = S_2$ defines the location of the interface (indicated by line c in the figure). The interface to the right of the liquid region is determined in a similar manner and is not shown. The relative proportion x_{l} of the liquid phase is then the normalized distance between the two Gibbs surfaces bounding the liquid. With this definition of the interface, the relation $\rho_{\text{l}} x_{\text{l}} + \rho_{\text{g}} x_{\text{g}} = \rho_{\text{ave}}$ holds by construction. Thus, for liquid–gas coexistence the lever rule remains valid even for small systems where the interfacial widths take a significant portion of the system dimension, as long as the size in the direction normal to the interface is large enough to fully include the interfacial region.

To determine the shear rates in the fast and slow bands and the location of the band

interface, we first obtained the flow field in the gradient direction by dividing the coordinate into 20 evenly spaced bins, calculated the average velocity in each layer, and connected these data points with a smooth curve by a polynomial fitting; the data and the fitted curves are shown in Fig. S7(a). To obtain the shear rate profile, we took the first derivative of the fitted flow field; the result is shown in Fig. S7(b). For steady state shear bands, we find two plateaus representing the shear rates in fast and slow bands, and two interfaces between these plateaus. The higher and lower plateau values are the local shear rates of fast and slow bands, respectively. To determine the location of the interface, we identify the midpoints of the higher and lower plateaus (points A and B in Fig. S7(b)), respectively. Similar to the Gibbs dividing surface[S14] in the liquid–gas coexistence, the boundaries between the fast and slow bands, d and e, are determined by the condition $S_1 = S_2$ and $S_3 = S_4$, respectively. Thus, the proportion of the fast x_f is the distance between d and e normalized by the gradient dimension. We have checked that $\dot{\gamma}_\mathrm{f} x_\mathrm{f} + \dot{\gamma}_\mathrm{s} x_\mathrm{s} = \dot{\gamma}$ holds.

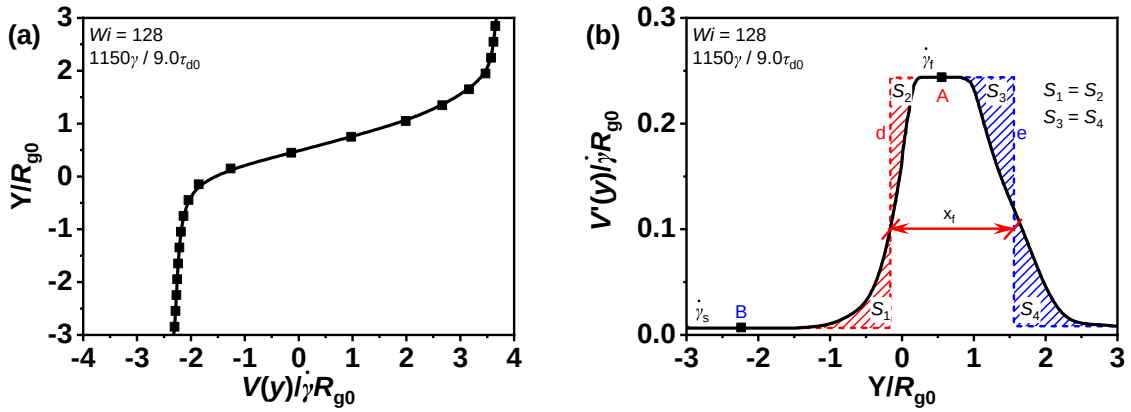

Figure S7: (a) Normalized velocity profile of a single sample at $Wi = 128$, $t = 9.0\tau_{\mathrm{d0}}$. The black squares are the simulation data and the smooth curve is obtained by polynomial fitting. (b) The corresponding normalized shear rate profile, where $V' = \partial V/\partial y$ is the local velocity gradient. The lines d and e are the Gibbs dividing surfaces, determined by the equal area conditions, $S_1 = S_2$ and $S_3 = S_4$.

S5 Same-sample correlation in the location of the maximum local shear rate at lower shear rates

Fig. S8 shows the location of the maximum local shear rate at $Wi = 128$ as the abscissa and the location of the maximum local shear rate at $Wi = 31.9$ as the ordinate after $\gamma = 20$ for each sample, with the sample number shown inside the symbol. More than half of the data fall near the diagonal, i.e., half of the interface locations for $Wi = 31.9$ are identical to those for $Wi = 128$ starting from the same microstate configurations, suggesting significant memory of the initial structure. The data that fall out of the diagonal are in part due to structural reconfiguration, and in part due to the presence of multiple shear bands which switched the roles between the fastest and the next fastest bands. The red symbols are the locations of the maximum rate in the next fastest bands.

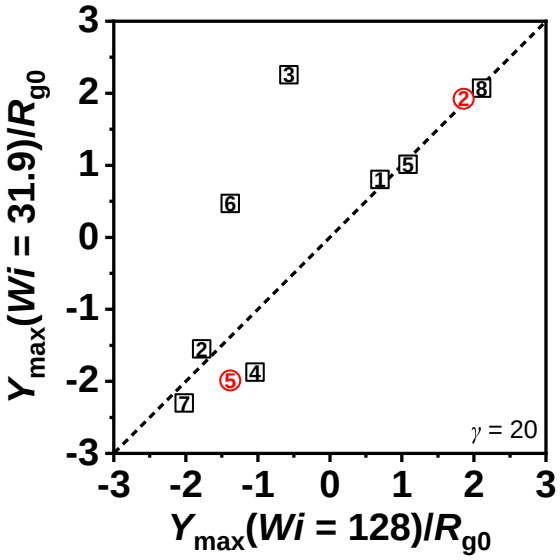

Figure S8: Same-sample correlation in the location of the maximum local shear rate in the fast band between shear rates $Wi = 128$ with $Wi = 31.9$ at $\gamma = 20$. Each sample corresponds to a distinct initial microstate configuration. The numbers inside the symbols correspond to sample numbers. For the same sample (i.e., same initial microstate configuration), the abscissa is the location of the maximum local shear rate in the fast band for $Wi = 128$ and the ordinate is that for $Wi = 31.9$. The black and red symbols represent the locations of the maximum shear rate in the fastest and next fastest bands, respectively.

S6 Chain end density and monomer density distribution

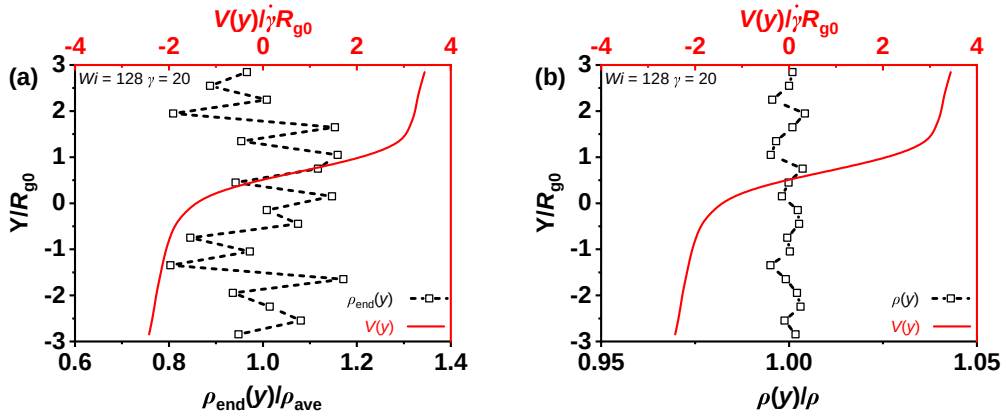

Figure S9: (a) Chain end density and (b) monomer density in different layers along the velocity gradient direction at $\gamma = 20$ with $Wi = 128$, and the corresponding velocity profile.

S7 Correlating the velocity profile with the kink number and first normal stress difference

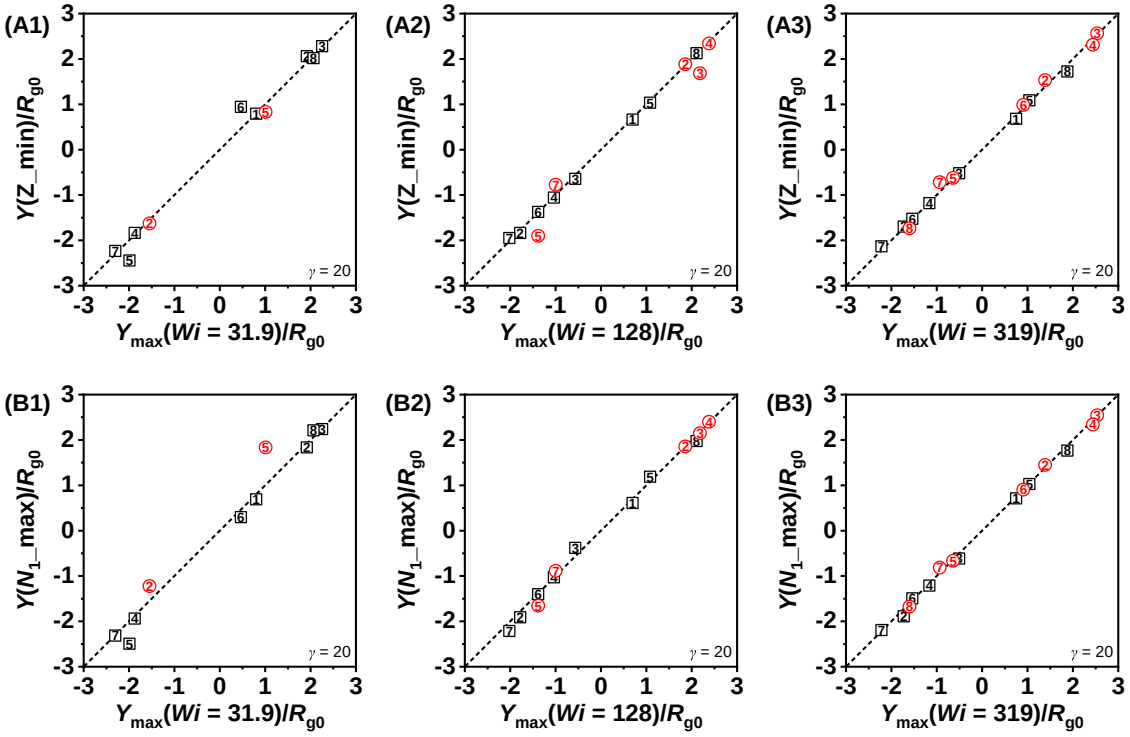

Figure S10: Correlations between the location of the maximum local shear rate in the fast band and the location of the minimum of Z_k (A1–A3), or the maximum of N_1 (B1–B3), at $\gamma = 20$ for $Wi = 31.9$, $Wi = 128$, and $Wi = 319$.

S8 Variation of shear rates in the fast and slow shear bands

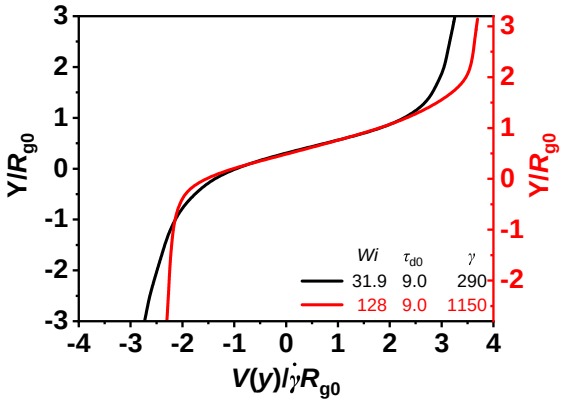

Figure S11: Normalized flow field for a single sample at $Wi = 31.9$ and 128 at $9\tau_{d0}$. The profile for $Wi = 128$ has been shifted vertically upward by $0.2R_{g0}$ to make the red and black lines overlap in the fast band.

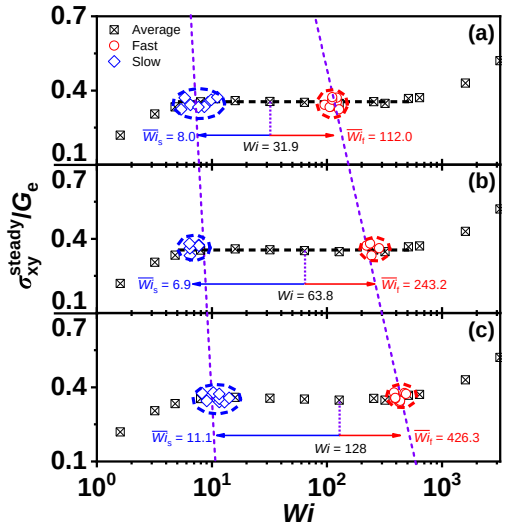

Figure S12: Variation of shear rates in the fast and slow shear bands. Each red (blue) symbol represents the shear rate and stress of fast (slow) band in a given sample with imposed shear rates $Wi = 31.9$, 63.8, and 128. $Wi_{f/s} \equiv \tau_{d0}\dot{\gamma}_{f/s}$. The definitions of $\dot{\gamma}_{f/s}$ are given in Section S4. The black crossed squares are the same data as shown in Fig. 1. For $Wi = 63.8$, the data used are the results from samples showing clear two-banded structures at $1.1\tau_{d0}$ (see Table S1). The purple dash lines are to guide the eyes.

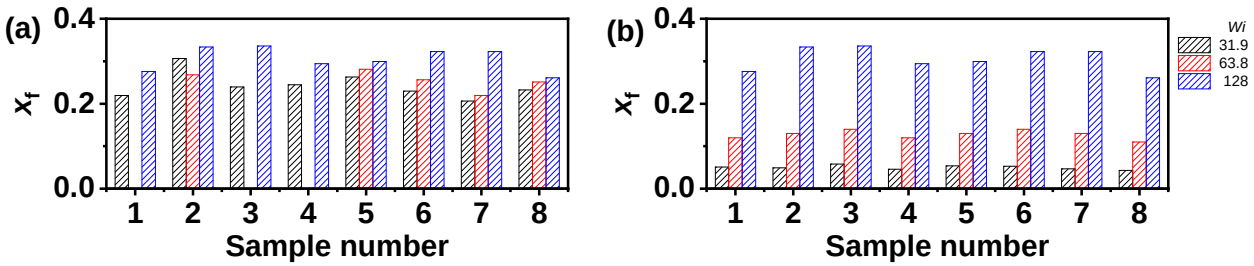

Figure S13: Relative proportion x_f of the fast band for all 8 independent samples at different shear rates. For $Wi = 63.8$, the data used are the results from samples showing clear two-banded structures at $1.1\tau_{d0}$, so there are fewer data in red. In (a), the actual data are shown as determined using the Gibbs dividing surfaces; in (b) we used data from $Wi = 128$ (Wi_f, Wi_s, and x_f) and the lever rule to predict x_f for the two other shear rates $Wi = 31.9$ and $Wi = 63.8$. The blue bars are the same as in (a). Clearly, the lever-rule predicted values of x_f for $Wi = 31.9$ and $Wi = 63.8$ are far smaller than the actual data, indicating violation of the lever rule. In fact, if we used data from $Wi = 31.9$, the predicted x_f would become greater than 1 for $Wi = 128$, which is clearly unphysical!

S9 Finite size effects

To ensure that the stress–strain curves and the correlations in the shear band locations reported in the main text with box size $6R_{g0} \times 6R_{g0} \times 4R_{g0}$ are not due to finite size effects, we also performed simulations using three larger box sizes $6R_{g0} \times 12R_{g0} \times 4R_{g0}$, $12R_{g0} \times 6R_{g0} \times 4R_{g0}$, and $6R_{g0} \times 6R_{g0} \times 8R_{g0}$ at $Wi = 128$ and 319. However, limited by computing resources, the simulations were run to $\gamma = 30$, and so we are unable to address possible finite size effects on properties of the steady-state shear bands.

The stress-strain curves for the different system sizes are very close to each other (Fig. S14). The increased box size also has no influence on the correlation in the location of the maximum local shear rate for different shear rates starting from the same microstate configurations (Fig. S15).

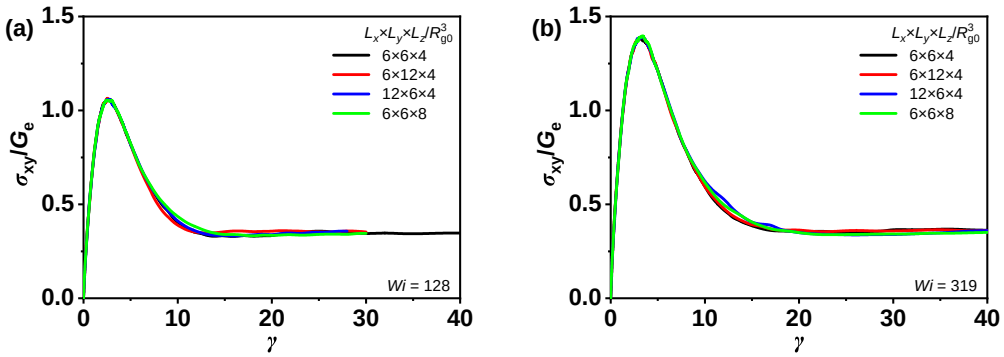

Figure S14: Stress vs. strain at (a) $Wi = 128$ and (b) $Wi = 319$ under different box sizes.

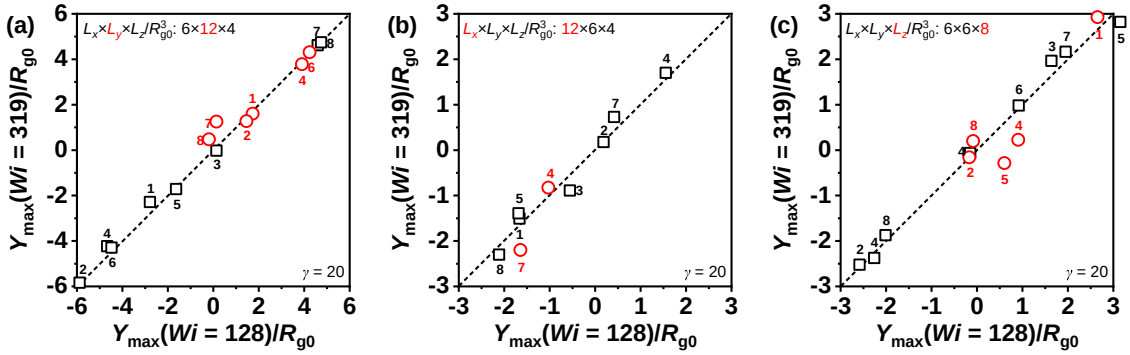

Figure S15: Same-sample correlation in the location of the maximum local shear rate in the fast band at $\gamma = 20$ with $Wi = 128$ vs. $Wi = 319$ under different box sizes. The number refers to the sample number. In (b), sample 6 is missing since we did not observe clear shear banding at $Wi = 319$.

S10 Description of movies

SI-movie1 and SI-movie2[S15] respectively show the motion of the center of mass (CM) of each polymer chain under the conditions of $Wi = 128$ (SI-movie1) and $Wi = 319$ (SI-movie2) in the xy plane with a window size of $6R_{g0} \times 6R_{g0}$ (box size), where the color contrast represents the difference between the velocity of CMs and their corresponding linear velocity, $\Delta v = v(y) - \dot{\gamma} y$

S11 Simulation results for the Mohagheghi–Khomami (MK) model

To resolve the discrepancy between our results and those by Khomami and coworkers[S16–S20], we ran simulations using their model system, which consists of 705 chains of length $N = 250$ at a monomer density of $\rho = 1.0 r_c'^{-3}$. The simulation box has an aspect ratio of 2.5 : 1 : 1 in the flow, gradient, and vorticity directions. All monomers are modeled

as beads interacting through pairwise repulsion force ($\boldsymbol{F}_{ij}$),

$$\boldsymbol{F}_{ij} = a\,(1 - r_{ij}/r'_{\rm c})\,\hat{\boldsymbol{r}}_{ij} \tag{S6}$$

where $a = 200k_{\rm B}T/r'_{\rm c}$ is the maximum repulsion between particles i and j, $r'_{\rm c}$ is the cut-off distance, and $\hat{\boldsymbol{r}}_{ij}$ is the unit vector. Chain connectivity is modeled by a harmonic potential between adjacent monomers on the chain,

$$U_{\rm harmonic} = 0.5k_{\rm h}(r_{ij} - r_{\rm eq})^2 \tag{S7}$$

the spring constant $k_{\rm h} = 400k_{\rm B}T/r'^2_{\rm c}$ and equilibrium bond length $r_{\rm eq} = 0.95r'_{\rm c}$. The bending potential has the same form as (Eq. S3) with $k_{\rm b} = 2k_{\rm B}T$. Mass (m), length ($r'_{\rm c}$), and energy ($k_{\rm B}T$) are taken as the basic units and set to be 1, and time unit is $\tau = (mr'^2_{\rm c}/k_{\rm B}T)^{1/2}$. The temperature is controlled by the DPD thermostat with dissipative force (Eq. S4), and random force (Eq. S5). The friction coefficient $\xi = 4.5$. The simulation time step is 0.012τ. The disengagement time $\tau_{\rm d0} = 1.0 \times 10^6\tau$ was given in Ref. S17. Stress in the steady state is the result of smoothing over 240τ. All simulations were performed on the LAMMPS platform and the data reported are results averaged over 8 independent samples. We used two different methods to equilibrate the system.

Method 1: Chains were initialized as random walks using the freely joined chain model. Simulation was run for $0.72\tau_{\rm d0}$ allowing for chain crossing (using a reduced $k_{\rm h} = 200$). The system was then run with the full model parameters for $8\tau_{\rm d0}$;

Method 2: Starting from linearly compressed chains in the flow direction (x) regularly arranged in the y-z plane, we turned on the full model parameters and ran the simulation for $8\tau_{\rm d0}$. This method was used by Khomami and coworkers according to an e-mail exchange from Dr. Khomami.

Within the error margins, these two equilibration methods result in the same static properties for $Z_{\rm k}$ and $R_{\rm g0}$ (Figs. S16(a) and (b)). Using the Z1 code, the kink number per

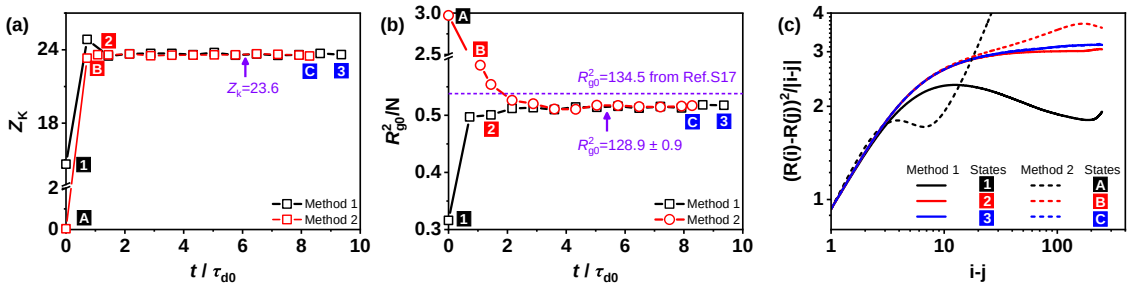

Figure S16: Evolution of (a) the kink number per chain Z_k and (b) the mean-square radius of gyration. Black and red lines correspond, respectively to Method 1 and Method 2. Dashed horizontal line is reported in Ref. S17. (c) Mean-square internal distance at different states corresponding to the numbers and letters shown in (a) and (b).

chain is $Z_{\rm k} = 23.6$. We additionally calculated the mean-square internal distances of polymer chains in 6 different states, as shown in Fig. S16(c), which suggests that the states 3 and C are fully equilibrated, state 2 is close to full equilibrium, and states 1, A and B are not. Henceforth, we will refer to state 3 or C as the fully equilibrated sample.

Since the stress minimum occurs at about $Wi = 40$ in the $\sigma_{xy}^{\rm steady}(\dot{\gamma})$ curve reported in Ref. S16, we first focus on this shear rate. In order to see the effect of the initial state on the steady-state stress, we compare the stress curves produced using various points in each protocol. Fig. S17(a) shows stress curves generated using states 1, 2, and 3 from Fig. S16, and Fig. S17(b) shows stress curves generated using states A, B, and C from Fig. S16. Even though states 2 and B are not yet fully equilibrated, the stress curves produced from these states are very close to those from the fully equilibrated samples. Strikingly, states 1 and A, which have not gone through any thermal equilibration, result in the same steady-state stress as those using the other samples, although the overshoot peaks produced from these nonequilibrium initial states are significantly lower. This suggests that the initial states have little effect on the steady-state stress for this shear rate. The discrepancy between our results and those of Khomami and coworkers in the $\sigma_{xy}^{\rm steady}(\dot{\gamma})$ curve is therefore unlikely due to differences in the sample preparation, although the differences in the static properties such as $R_{\rm g0}$ and Z_k are still puzzling.

Ref. S18 provides the stress–strain curve for $Wi = 1$, 10, 30, and 100. As a further test, we tried to reproduce these stress curves using our equilibrated sample (state 3). In Fig. S17(c)

we show our results as the solid lines, and the MK results as the symbols connected by dashed lines. We see good agreement for $Wi = 1$, 10, and 100, but their result for $Wi = 30$, which is close to the stress minimum reported in Ref. S16, lies significantly below ours throughout the entire shear history.

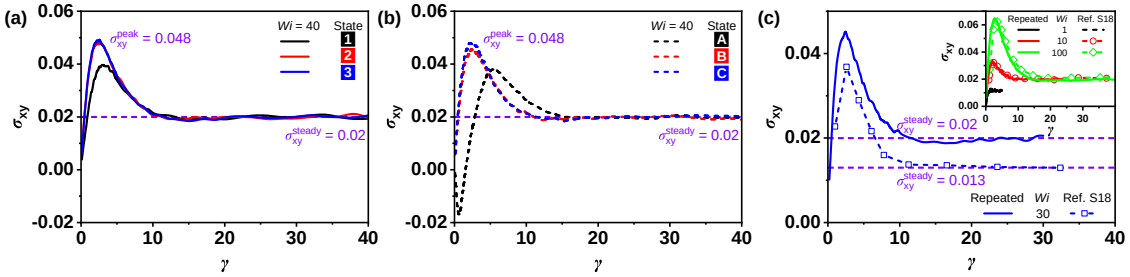

Figure S17: Stress–strain curves at shear rate $Wi = 40$ produced from (a) states 1, 2, and 3 and (b) states A, B, and C. (c) Comparison of stress–strain curves from our simulation with results reported in Ref. S18 for $Wi = 1$, 10, 30, and 100. Note that for $Wi = 1$, we used state 2 as the initial state. Data from Ref. S18 were reproduced with permission from The Society of Rheology, Copyright 2016.

In Fig. S18(a), we show the $\sigma_{xy}^{\text{steady}}(\dot{\gamma})$ curve we obtained from using the MK model, and compare with their results for both the monodisperse[S16] and polydisperse[S20] systems from the work of Khomami and coworkers. It is clear that our results (black dots) do not show the pronounced minimum exhibited by the data reported in Ref. S16 for the monodisperse systems (red circles) but instead a stress plateau. However, our results are similar to those reported for the polydisperse system (red cross-circles).[S20] We note that Ref. S16 used their own in-house code, while for the polydisperse system, Ref. S20 used LAMMPS. Finally, we show that the correlation in the band interface location between different shear rates as shown in Fig. 3 of the main text also exists in the MK model. Fig. S18(b) demonstrates the correlation in the interface location between $Wi = 40$ and $Wi = 100$ at $\gamma = 20$ for the MK model, starting from the same microstate configurations.

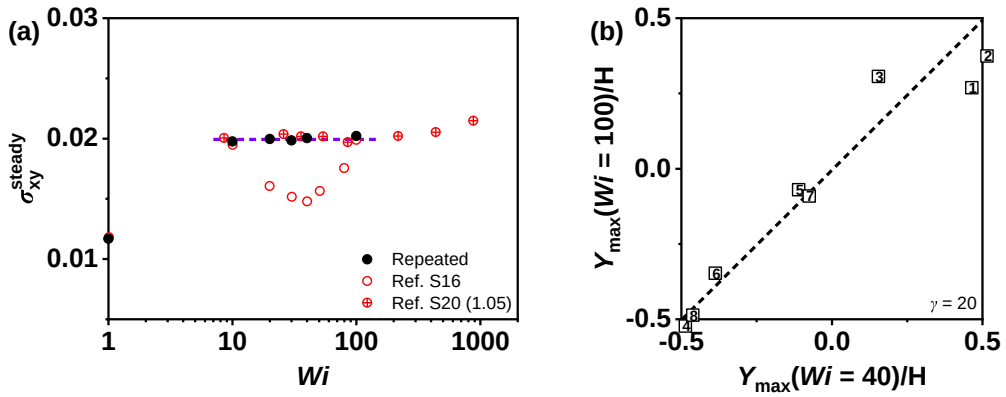

Figure S18: (a) The $\sigma_{xy}^{\text{steady}}(\dot{\gamma})$ curve for the MK model with $N = 250$. The black dots are results from our simulation using this model. Result for $Wi = 1$ was obtained starting from state 2 in Fig. S16(a). Red circles are results reported in Ref. S16 for the monodisperse system, and red cross-circles are results reported for the polydisperse system with PDI=1.05 in Ref. S20. Data from Ref. S16 were reproduced with permission from The American Chemical Society, Copyright 2015; Data from Ref. S20 were reproduced with permission from The Royal Society of Chemistry, Copyright 2020. (b) Same-sample correlation in the location of the maximum local shear rate in the fast band at $\gamma = 20$ with $Wi = 40$ vs. $Wi = 100$.

References

(S1) Kremer, K.; Grest, G. S. Dynamics of entangled linear polymer melts: A molecular dynamics simulation. *J. Chem. Phys.* **1990**, *92*, 5057–5086.

(S2) Auhl, R.; Everaers, R.; Grest, G. S.; Kremer, K.; Plimpton, S. J. Equilibration of long chain polymer melts in computer simulations. *J. Chem. Phys.* **2003**, *119*, 12718–12728.

(S3) Soddemann, T.; Dunweg, B.; Kremer, K. Dissipative particle dynamics: A useful thermostat for equilibrium and nonequilibrium molecular dynamics simulations. *Phys. Rev. E* **2003**, *68*, 046702.

(S4) Cao, J.; Likhtman, A. E. Shear banding in molecular dynamics of polymer melts. *Phys. Rev. Lett.* **2012**, *108*, 028302.

(S5) Tretyakov, N.; Müller, M.; Todorova, D.; Thiele, U. Parameter passing between molec-

ular dynamics and continuum models for droplets on solid substrates: The static case. *J. Chem. Phys.* **2013**, *138*, 064905.

(S6) Baig, C.; Mavrantzas, V. G.; Kröger, M. Flow effects on melt structure and entanglement network of linear polymers: Results from a nonequilibrium molecular dynamics simulation study of a polyethylene melt in steady shear. *Macromolecules* **2010**, *43*, 6886–6902.

(S7) Likhtman, A. E.; McLeish, T. C. B. Quantitative theory for linear dynamics of linear entangled polymers. *Macromolecules* **2002**, *35*, 6332–6343.

(S8) Shaffer, J. S. Effects of chain topology on polymer dynamics: Bulk melts. *J. Chem. Phys.* **1994**, *101*, 4205–4213.

(S9) Ravindranath, S.; Wang, S.-Q.; Olechnowicz, M.; Quirk, R. P. Banding in simple steady shear of entangled polymer solutions. *Macromolecules* **2008**, *41*, 2663–2670.

(S10) Adams, J. M.; Fielding, S. M.; Olmsted, P. D. Transient shear banding in entangled polymers: A study using the Rolie-Poly model. *J. Rheol.* **2011**, *55*, 1007–1032.

(S11) Johnson, J. K.; Zollweg, J. A.; Gubbins, K. E. The Lennard-Jones equation of state revisited. *Mol. Phys.* **1993**, *78*, 591–618.

(S12) Shinoda, W.; Shiga, M.; Mikami, M. Rapid estimation of elastic constants by molecular dynamics simulation under constant stress. *Phys. Rev. B* **2004**, *69*, 134103.

(S13) Watanabe, H.; Ito, N.; Hu, C.-K. Phase diagram and universality of the Lennard-Jones gas-liquid system. *J. Chem. Phys.* **2012**, *136*, 204102.

(S14) Hansen, J.-P.; McDonald, I. R. *Theory of Simple Liquids: with Applications to Soft Matter*, 4th ed.; Academic Press, 2013.

(S15) Alexander, S. Visualization and analysis of atomistic simulation data with OVITO-the open visualization tool. *Modelling Simul. Mater. Sci. Eng.* **2010**, *18*, 015012.

(S16) Mohagheghi, M.; Khomami, B. Molecular processes leading to shear banding in well entangled polymeric melts. *ACS Macro Letters* **2015**, *4*, 684–688.

(S17) Mohagheghi, M.; Khomami, B. Elucidating the flow-microstructure coupling in the entangled polymer melts. Part I: Single chain dynamics in shear flow. *J. Rheol.* **2016**, *60*, 849–859.

(S18) Mohagheghi, M.; Khomami, B. Elucidating the flow-microstructure coupling in entangled polymer melts. Part II: Molecular mechanism of shear banding. *J. Rheol.* **2016**, *60*, 861–872.

(S19) Mohagheghi, M.; Khomami, B. Molecularly based criteria for shear banding in transient flow of entangled polymeric fluids. *Phys. Rev. E* **2016**, *93*, 062606.

(S20) Boudaghi-Khajehnobar, M.; Edwards, B. J.; Khomami, B. Effects of chain length and polydispersity on shear banding in simple shear flow of polymeric melts. *Soft Matter* **2020**, *16*, 6468–6483.